Enhancement of the Curie temperature in NdBaCo_{2}O_{5.5} by A-site Ca substitution

S. Kolesnik, B. Dabrowski, O. Chmaissem, S. Avci, J. P. Hodges, M. Avdeev, and K. Świerczek

Enhancement of the Curie temperature in NdBaCo$_2$O$_{5.5}$ by A-site Ca substitution

S. Kolesnik,[1,*] K. Świerczek,[1,2,#] O. Chmaissem,[1,2] S. Avci,[2] J. P. Hodges,[3] M. Avdeev,[4] and B. Dabrowski[1,2]

[1] Physics Department, Northern Illinois University, DeKalb, IL 60115, USA

[2] Materials Science Division, Argonne National Laboratory, Argonne, IL 60439, USA

[3] Spallation Neutron Source, Oak Ridge National Laboratory, Oak Ridge TN 37831, USA

[4] Bragg Institute, Australian Nuclear Science and Technology Organization, Menai, NSW 2234, Australia

[#] Permanent address: AGH University of Science and Technology, Faculty of Energy and Fuels, Department of Hydrogen Energy, al. A. Mickiewicza 30, 30-059 Kraków, Poland

[*] Corresponding author. E-mail: kolesnik@niu.edu

Abstract

Layered cobaltites RBaCo$_2$O$_{5.5}$ (R=rare earth and Y) undergo a sequence of magnetic and electronic transitions between antiferromagnetic/ferrimagnetic/paramagnetic and insulating/paramagnetic metallic states with respective transition temperatures T_N (~230-260 K) $<T_C$ (~250-290 K) $<T_{MI}$ (~360 K). We have synthesized a Nd$_{1-x}$Ca$_x$BaCo$_2$O$_{5.5}$ series (0≤x≤0.2) of cation- [(Nd,Ca)/Ba] ordered and oxygen vacancy ordered materials and investigated them by neutron diffraction, magnetization, electronic and thermal transport. We observe that upon Ca doping T_N is decreasing to 0 for x=0.1 and T_C is increasing and coincides with T_{MI} for x>0.12, which weakly changes with Ca substitution from ~360 to ~340 K. This is the largest enhancement of T$_C$ observed for these cobaltites. Unlike hole doping by adding oxygen, the Ca doping does not disrupt the cation and oxygen vacancy orderings up to x=0.20.

I. Introduction

Layered cobaltites $R\text{BaCo}_2\text{O}_{5+\delta}$ (R=rare earth and Y) have been studied over the last several years due to interesting magnetic and electronic properties resulting from the R/Ba cation ordering along the c-axis in addition to several kinds of oxygen vacancy orderings, which depend on oxygen content.[1-15] The oxygen content can be changed over a wide range from $5+\delta = 5.0$ to 5.8 [6], which changes the ground states of these materials from the charge-ordered antiferromagnetic (AFM) insulator for $\delta = 0$ to the optimally doped band insulator for $\delta = 0.5$, and to the heavily hole-doped metallic ferromagnetic state for $\delta > 0.7$. The particular doping level $\delta = 0.5$ is associated with an oxygen vacancy ordering, which manifests itself as alternating planes of CoO_6 octahedra and CoO_5 square pyramids along the a-axis of the crystal structure, each containing one Co^{3+} ion. These optimally doped $R\text{BaCo}_2\text{O}_{5.5}$ compositions demonstrate a variety of unique temperature-dependent physical phenomena, such as dramatic change of the electronic properties (the Seebeck coefficient), metal insulator transition at T_{MI} (~360 K), the Co^{3+} spin state transition, Co^{3+} spin state ordering at low temperatures, ferrimagnetism below T_C (~250-290 K) and antiferromagnetism below T_N (~230-260 K) $< T_C$. In a seminal paper, Taskin et al. observed that these properties are strongly dependent on even a slight oxygen non-stoichiometry.[6] Complex properties have been associated with the varying spin state of the cobalt, which often behaves in unpredictable ways depending on the chemical composition of the investigated material and the specificity of the Co local environment.[6] Thus, consideration of Co^{3+} and Co^{4+} ions with high, intermediate and low spin states is frequently required to explain the observed behavior, however, offering also an additional degree of freedom when designing new materials with tunable properties. Recent studies also suggest that an assignment of a unique charge state to Co based on chemical formula may not be possible, introducing an additional complication.[7] $R\text{BaCo}_2\text{O}_{5+\delta}$ is one of the most fascinating cobaltite systems because it offers several possibilities for diverse chemical substitutions at the distinct R, Ba and Co sites, in addition to varying oxygen content. The substituting ions may have various sizes and oxidation states and therefore would act as a control parameter for

modifying structural distortions and injecting or removing charges from the system without severely changing the local oxygen environment around the Co ions.

While there are several studies of the RBaCo$_2$O$_{5+\delta}$ compounds with variable oxygen contents causing conversion of the CoO$_5$ pyramids to CoO$_6$ octahedra for $\delta > 0.5$ (or vice versa for $\delta < 0.5$), the information about the cation substitutions in these materials with controlled oxygen content is scarce. Isovalent Ca substitution for Ba destroys the AFM long-range order and stabilizes the ferrimagnetic (FM) state.[16] Substitution of Ni for Co in GdBaCo$_{2-x}$Ni$_x$O$_{5+\delta}$ strongly suppresses all the transition temperatures, [17] while Fe substitution leads to phase separation of GdBaCo$_2$O$_{5.5+\delta}$ into Fe-rich and Fe-free regions.[18]

A particular case of substitution of heterovalent Ca for R is especially interesting because while its effect on the crystal lattice of R_{1-x}Ca$_x$BaCo$_2$O$_{5+\delta}$ is small due to the similar ionic sizes of R and Ca, it affects the magnetic properties in various ways depending on the size of R. The substitution for smaller size R = Dy and Ho causes large deterioration of the long-range magnetic ordering in the system, ultimately leading to a paramagnetic state for x $\geq$ 0.2.[19] The substitution for intermediate-size europium expands drastically the range of ferromagnetic phase down to 10 K and increases T_C up to 320 K, but does not affect the metal–insulator transition temperature.[20] For other intermediate-size R ions (Y, Gd, and Sm) similar behavior is observed indicating a correlation of T_C to the ionic size of R.[21] All these Ca substituted materials were synthesized in air and, therefore, their oxygen content could possibly be noticeably different from 5.5, which may contribute to the observed phenomena.

In this work we describe the structural, transport, and magnetic properties of the nearly stoichiometric system Nd$_{1-x}$Ca$_x$BaCo$_2$O$_{5.5}$ with $0 \leq x \leq 0.2$. We show enhanced ferrimagnetism and preservation of the metal to insulator transition in the entire substitution range. Also, it is observed that hole doping by the substitution of Ca^{2+} for R^{3+} when the pyramidal and octahedral coordinations are preserved leads to different effects than the hole doping by excess oxygen in GdBaCo$_2$O$_{5+\delta}$, which changes the Co coordination to oxygen.[6] With substitution of Ca^{2+}, a wider range of homogenous charge doped samples has been achieved than with oxygen doping showing rapid decrease of T_N to 0 for x=0.1 and weak decrease of T_{MI} from ~360 to ~340 K for x = 0.2.

3

Dissimilar to hole doping by oxygen, the hole doping in $Nd_{1-x}Ca_xBaCo_2O_{5.5}$ induces a systematic increase of resistivity and an increase of T_C up to 340 K the highest observed for these cobaltites.

II. Synthesis and Experimental Techniques

Polycrystalline $Nd_{1-x}Ca_xBaCo_2O_{5.5}$ samples in the $0.0 \leq x \leq 0.2$ range were synthesized by the solid state reaction of appropriate amounts of Nd_2O_3 (dried in air), Co_3O_4, $CaCO_3$ and $BaCO_3$ (all > 99.99% purity). Reactants were thoroughly mixed in an agate mortar and fired in air several times in the $900 - 1150$ ^{o}C range with intermediate grindings. The reaction was monitored with x-ray diffraction measurements, performed after each step of the synthesis procedure using a Rigaku D/MAX powder diffractometer in the $20 - 70$ degrees range with $Cu_{K\alpha}$ radiation. After achieving single-phase samples the final step of the synthesis procedure was balancing the oxygen content by annealing in ultrapure argon gas at 390 °C for 3 days. Partial pressure of oxygen was kept at less than 20 ppm. After firing in argon gas at 390 °C, our samples were cooled to room temperature by turning off the furnace (natural furnace cooling at ~ 3 deg/min at 300 °C and a slower rate at lower temperatures.)"

Thermogravimetric analysis (TGA) was performed on a Cahn TG171 thermobalance in several flowing gas mixtures up to 1100 ^{o}C to determine the oxygen stoichiometry as a function of oxygen pressure and temperature, and to determine the exact oxygen content of the final samples. The weight of the approximately 1 gram samples was measured with a 5 μg precision. Oxygen content in the samples was determined by the weight difference between the initial sample and the total reduction products Nd_2O_3, BaO, CaO and metallic Co obtained by slow reduction in 42% hydrogen/argon atmosphere (1 deg/min) up to the point of no weight change. Typical TGA results are presented in Fig. 1. Fig. 1(a) shows heating and cooling data in pure oxygen for a starting sample $Nd_{0.94}Ca_{0.06}BaCo_2O_{5.51\pm0.01}$ obtained from annealing in ultrapure argon gas at 360 °C for 3 days. On heating, the sample absorbs oxygen at relatively low temperatures of 200-300 °C. Further heating to higher temperatures of 500 °C results in the release of some oxygen, which is readily reabsorbed on cooling,

indicating fast surface and bulk oxygen exchange at these temperatures. Cooling to room temperature results in final oxygen content of 5.78. Subsequent heating in Ar results in fast release of oxygen with a characteristic narrow plateau near 390 °C, which indicates the presence of an enhanced stability of oxygen composition at 5.50. Similar experiments were conducted to determine the annealing conditions necessary for obtaining samples with stoichiometric oxygen content 5.50. The total oxygen content of all samples was determined by slow reduction in 42% hydrogen/argon atmosphere, an example of which is shown in Fig. 1(b) for the starting sample $Nd_{0.84}Ca_{0.16}BaCo_2O_{5.50\pm0.01}$ obtained from annealing in ultrapure argon gas at 390 °C for 3 days. The oxygen content of the remaining $Nd_{1-x}Ca_xBaCo_2O_{5.5}$ samples was confirmed to be 5.50 within the experimental error of about 0.01. Overall starting and final cation compositions have been confirmed by energy dispersive x-ray spectroscopy on a Hitachi S-4700 electron microscope at the Electron Microscopy Center, Argonne National Laboratory.

Room temperature neutron powder diffraction experiments were performed at room temperature at the Oak Ridge National Laboratory Spallation Neutron Source ($0 \leq x \leq 0.16$) and at the Australian Bragg Institute ($x = 0.18, 0.20$). Time-of-flight data were collected at the high-resolution diffractometer (POWGEN) [22] whereas a constant wavelength of 2.4395 Å was selected for the $x = 0.18, 0.20$ experiments (Echidna). Structural refinements were performed by the Rietveld method with the GSAS/EXPGUI suite of programs. [23] In all refinements, the background was modeled using a shifted Chebyschev polynomial with 16 refinable parameters. For Echidna, the profile function was modeled using the modified Thomson-Cox-Hasting pseudo-Voigt function (TCHZ) with anisotropic broadening. For POWGEN, Von Dreele's exponential pseudovoight convolution profile function was used. Significant deviations of the refined structural parameters (not shown in further analysis) for $x = 0.20$ suggested that the solubility limit was reached for that composition.

The dc magnetization was measured using a Magnetic Property Measurement System Model MPMS-7 (Quantum Design). The temperature dependence of magnetization was measured in the temperature range 5-600 K on cooling in a magnetic field of 1 kOe. From that, the Curie temperature, the Néel temperature, and the properties

of the paramagnetic state were determined. Isothermal magnetization hysteresis loops were measured at several temperatures in magnetic fields up to 70 kOe. Electrical resistivity, thermal conductivity, and the Seebeck coefficient were all measured using a Physical Property Measurement System Model 6000 (Quantum Design).

III. Results and discussion

IIIa. Crystal structure

At room temperature, the nuclear structure of the non-substituted parent material, $NdBaCo_2O_{5.5}$, has widely been described as crystallizing in the orthorhombic Pmmm space group with unit cell dimensions on the order of a_p x $2a_p$ x $2a_p$, where a_p is the lattice parameter of a simple ABO_3 perovskite structure. The doubling of the b-axis arises from the alternation of ordered octahedral and pyramidal cobalt sheets. The pyramidal layers form by the corner-shared coupling of oppositely oriented pairs of cobalt pyramids. In turn, the pyramidal pairs promote the ordering of Nd and Ba on independent and alternating layers; thus, doubling the c-axis as well. In the Ba layers, oxygen atoms fully occupy their crystallographic sites, whereas significant vacancies and oxygen/vacancy ordering take place in the Nd layers. On the other hand, the remaining perfectly ordered oxygen atoms, O3, serve as apices for the corner-sharing CoO_6 octahedra.

At low temperature, it was noted that $RBaCo_2O_{5.5}$ materials exhibit ferrimagnetic properties as suggested by the unexpected weak ferromagnetic signal. From a structural point-of-view, ferrimagnetism would be expected when two ferromagnetic sublattices (of different magnitudes) would couple antiferromagnetically along a particular direction. A weak ferromagnetic signal could also arise from the cooperative canting of antiferromagnetically ordered magnetic moments. For $RBaCo_2O_{5.5}$, the low temperature magnetic structures have all been associated with the appearance of superstructure peaks that require the doubling of the a-axis to form a superlattice of dimensions $2a_p$ x $2a_p$ x $2a_p$ [12], see Fig. 2. In this work, we were successful in driving the magnetic transition to temperatures at or above 300 K by simple chemical substitution of Ca at the Nd sites. While there is a general agreement concerning the size of the superstructure unit cell, the magnetic structures and corresponding space group symmetries remain debatable.

6

However, we note here that determining the exact magnetic symmetry for our calcium substituted samples will not be attempted in the present work because our neutron data collected at room temperature only contain weak magnetic peaks. Plans to collect neutron data at low and high temperatures are currently being pursued.

To summarize our current understanding of the structure of RBaCo$_2$O$_{5.5}$, we first note that the $2a_p$ x $2a_p$ x $2a_p$ superstructure must be a subgroup of the parent Pmmm structure induced by subtle distortions associated with Ca substitution and/or the long range ordering of the Co magnetic moments. A total of eight subgroup models consistent with the doubling of the a-axis (k-point x) is possible using the symmetry operators ofspace groups Pmmm, Pmma, Pmam and Pmaa. Pmam is essentially the same as Pmma but the permutation of the symmetry elements allows for the splitting of different atoms on independent sites. The four space groups allow structural models with the origin located at (0,0,0) or shifted to (1/2, 1/2, 0). Each of these eight models allows distinct displacive modes but of particular interest to this workis the difference in the number of independent cobalt, Nd(Ca) and Ba, and/or oxygen sites. Satisfactory agreement factors were obtained using the published Pmma model (Pmma-1) in addition to two other models, namely Pmma-2 with its origin shifted to match that of the parent Pmmm structure and Pmaa.

Relying on single crystal x-ray diffraction and group theory considerations, Chernyshov et $al.$ [24] proposed a model based on the Pmma symmetry in which the origin of the unit cell was shifted to (1/2, 1/2, 0) with respect to Pmmm in order to split the cobalt ions into four independent sites (two octahedral and two pyramidal sites). With this choice, the cobalt ions are allowed to have four independent magnetic moments of different magnitudes and orientations that may explain the observed weak magnetic signal. Additional splitting of the oxygen atoms is also required. Our refinements using this model were difficult to converge without the introduction of extensive structural constraints and severe damping of all the refined variables. Plots of the internal bond-lengths and bond-angles as a function of increased calcium content unveiled the erratic behavior of severe structural distortions from which no physical trends could be extracted.

Shifting the origin back to that of P*mmm* (P*mma-2*) or using the new space group P*maa* reduces the number of independent Co sites to only two. In P*mma-2*, splitting of two oxygen sites would be required whereas, in P*maa*, the splitting of only one oxygen site was needed and the refinements converged immediately without any constraints or damping. It must be noted, however, that all three models produced similar agreement factors and best-fit Rietveld plots. Plots shown in Fig. 3 were obtained using the P*maa* model. On the other hand, the magnetic structure refined in all the three models produce a perfectly aligned G-type antiferromagnetic sublattice that is not capable of explaining any ferrimagnetism. At room temperature, the observed ferrimagnetic signals of ~0.1-0.2 μ_B are significantly below the typical neutron detection limit of ~0.3-0.5 μ_B.

As described above, the agreement factors alone cannot be used to discriminate against one model or another; however, the smoothly varying internal bond-lengths and bond-angles obtained with the P*maa* candidate lead us to choose this space group as suitable for describing the nuclear symmetry. The magnetic symmetry, which is not necessarily the same as the nuclear symmetry, will be dealt with after collecting low temperature data with significant magnetic intensities. However, for this work, the weak magnetic intensities were fit using the symmetry of the magnetic space group *Pmaa'*. Removing the time reversal symmetry of the second a-glide allows the construction of a G-type antiferromagnetic structure in which two distinct magnetic moments for Co1 and Co2 can be refined. The magnetic moments lie parallel to the a-axis with no canting allowed by symmetry in any other direction. Each spin (e.g., for Co1) is antiferromagnetically coupled with six (4 Co1 and 2 Co2) nearest neighboring spins. Likewise, each Co2 spin couples antiferromagnetically with 4 Co2 and 2 Co1 spins. The refined magnetic moments, M_x, are shown in Fig. 4(c) and listed in Table II for the $0.08 \leq x \leq 0.18$ (i.e., samples with discernible magnetic peaks at room temperature). Representative best-fit-Rietveld refinements are presented in Fig. 3 for the x = 0 and 0.16 samples.

The structural results presented in Tables I and II were obtained with the assumption that the oxygen sublattice ($O_{5.5}$) is perfectly ordered. As some degree of oxygen disorder is to be realistically expected as discussed in Refs. [25-27], we have investigated the possibility that the site of the O3 octahedral apices may not be fully

occupied and that the otherwise "missing" oxygen would partly occupy the available vacancy sites within the pyramidal sheets. This situation would depict some degree of disorder in the otherwise perfectly ordered network of octahedral and pyramidal cobalt. For all the samples, the fractional occupancy of O3 refined to within the range 0.90-0.99 (±0.03); thus, essentially indicating full site occupancy within one to three standard deviations which is in good agreement with the TGA hydrogen reduction results described and shown in the previous section. No extra oxygen was found, as expected for perfectly oxygen ordered materials, in any quantity at the vacant sites between the pyramids. All the remaining main frame oxygen atoms refined to full occupancy within one or two standard deviations on their respective sites (i.e., O1, O2, O4, O5, O6 and, when present, O7) and therefore they were kept fixed during the final refinements. We conclude that our samples exhibit perfect long range oxygen ordering consistent with the alternating pyramidal and octahedral structural sheets shown in Fig. 2.

As shown in Fig. 4, the substitution of Nd^{3+} (10 coordinated) by the slightly larger Ca^{2+} ions results in a negligible effect on the lattice parameters and unit cell volume. This unexpected result may be explained by the opposite effects on the lattice generated by the increase of the valence of Co cations above 3+ (i.e., by the formation of smaller Co^{4+} ions). At x = 0.18, the average Co oxidation state would be 3.09 indicating that only slight hole doping takes place by the calcium substitution in the $0 \leq x \leq 0.18$ range. Therefore, it is very difficult to obtain systematic trends in the behavior of the Co-O bond-lengths as a function of increasing Ca content. Nonetheless, we note that these bonds remain flat on average with a very slight trend towards shorter average values for higher Ca concentrations. For the magnetic $x \geq 0.08$ samples, we note an abrupt change in the Co-O bond lengths connecting the Co pyramids to the Co octahedra (namely Co-O6 and Co-O7). At the same time, the initially 180° apical O2-Co1-O3 bond angle buckles by a few degrees seemingly in response to the long range ordering of the cobalt magnetic moment. The local environment around the pyramidal cobalt ions remains largely unaffected. Our data suggest that hole-doping primarily takes place at the octahedral Co1 sites. Evolution of the refined Co1 and Co2 magnetic moments is shown

in Fig. 4. Tables I and II list the most relevant crystallographic information and the corresponding bond-lengths and angles for the whole series.

IIIb. Electrical and thermal transport properties

Temperature dependences of the Seebeck coefficient α, the electrical resistivity ρ, and thermal conductivity κ are presented in Fig. 5. The Seebeck coefficient at temperatures below T_{MI} (100-300 K) is large and positive, which points at a slightly hole-overdoped state for all the compositions in the entire Ca substitution range. This observation is in agreement with the results of the TGA analysis and diffraction data. The low-temperature Seebeck coefficient decreases with x similar to the hole doping by oxygen in single-crystals of $GdBaCo_2O_{5+\delta}$.[6] At these temperatures, the resistivity is semiconducting and roughly increases with an increase in Ca content. This trend is opposite to the observed decrease of resistivity upon hole doping within the same doping range in $GdBaCo_2O_{5+\delta}$.[6]. In the latter case, the resistivity decreases with increasing δ and eventually becomes of metallic character for $\delta > 0.7$. The difference may arise from structural causes such as a more conducting 3-dimensional Co-O network with larger amount of CoO_6 octahedra for $\delta > 0.5$. In addition, we note that our resistivity values are considerably larger than measured for single-crystals of $GdBaCo_2O_{5+\delta}$ with the difference increasing at decreasing temperatures indicating considerable contribution of grain boundary scattering resistivity in polycrystalline samples. The combination of the measured transport properties gives the thermoelectric figure of merit $ZT = \alpha^2 T/\kappa\rho \sim$ 0.02, which attains maximum values close to RT for low Ca contents (0.04-0.10). Taking into account decreased electrical conductivity in our polycrystalline samples these ZT's should be considered as the lower estimates of achievable values.

At the MIT temperature T_{MI}, a characteristic drop in resistivity is observed. The resistivity values (10^{-2}-10^{-3} Ωcm), right above T_{MI} are lower by more than an order of magnitude than below T_{MI} although the temperature dependence is not strictly metallic. Nevertheless, we will use the term MIT commonly used to describe this transition in layered cobaltites. A hysteresis of a few degrees in resistivity can be observed at T_{MI} for the entire family of $Nd_{1-x}Ca_xBaCo_2O_{5.5}$ samples confirming first order transition. The

10

resistivity above T_{MI} also increases with increasing x (it decreases with increasing δ in GdBaCo$_2$O$_{5+δ}$ single-crystals). At the same characteristic temperature, a pronounced drop in the Seebeck coefficient and a significant jump in thermal conductivity κ are observed, which point to correlated changes of the electronic and thermal transport at T_{MI}. In Fig. 5(c), we present the electronic part of the thermal conductivity, calculated according to the Wiedemann-Franz relationship $κ_E=L_0σT$, where $L_0 = 2.45 \ 10^{-8}$ W Ω/K^2 is the Lorenz number and σ is the electrical conductivity. The electronic thermal conductivity is small compared to the lattice thermal conductivity below T_{MI}, but increases significantly above T_{MI}. The magnitudes of the change in electronic and lattice thermal conductivities across T_{MI} are comparable, which underscores the coupling between the thermal and electronic properties at the transition. For x = 0, the size of the jump of the electronic part of the thermal conductivity is about 0.5 W/Km. The drop of the Seebeck coefficient and a change of its sign above T_{MI} in pure RBaCo$_2$O$_{5.5}$ has been interpreted as a spin blockade effect.[28]

In Fig. 6(a), the Seebeck coefficient α at several temperatures is plotted as a function the Ca concentration x, which is nominally twice amount of the hole doping per Co. A decrease of α with Ca doping is similar to a decrease of α with increased oxygen content in RBaCo$_2$O$_{5.5+δ}$ (full circles: data taken from Ref. 6). In the latter case, one oxygen ion per formula unit introduces two holes, so the Ca substitution and doping levels are related by x = δ/2. The large and positive α at T = 100-300 K (below T_{MI}) becomes small above T_{MI} and shows a change of sign only for small x [Fig. 6(b)]. If a simple Coulomb blockade picture was adopted, in which the negative α is related to the hopping of electrons from Co^{2+}, created by charge disproportionation of Co^{3+}, we should observe that above ~x = 0.06, the low values of α in the "metallic" state are positive, which would indicate that the increased concentration of delocalized Co^{4+} holes dominates the electrical transport also above T_{MI}. The electrical resistivity of Nd$_{1-x}$Ca$_x$BaCo$_2$O$_{5.5}$ [Fig. 6(c)] is a complicated function of hole doping. In general, it increases with x, but this increase is non-monotonic, at low temperatures ~100 K, the resistivity demonstrates thermally activated behavior $ρ(T)=\exp(E_g/k_BT)$, where E_g is the activation energy, k_B is the Boltzmann constant. The determined values of E_g are presented in [Fig. 6(d)].

In further analysis we attempted to follow the approach by Jonker [29] applied previously to RBaCo$_2$O$_{5.5}$ below [6] and above [7] T_{MI}, as well as to other mixed conductors [30]. That approach describes systems, in which two-carrier (hole and electron) transport is present. For RBaCo$_2$O$_{5.5}$ material on the boundary between these two conduction mechanisms this approach should be suitable to apply. The balance between hole and electron conductivities determines a relation between the Seebeck coefficient α and the electrical conductivity σ. This relation in the Jonker approach is described as a universal pear-shape curve, which in the extrinsic regime (for high conductivities) predicts a linear relation $\alpha=(k_B/e)\ln\sigma$. This relation was observed in Ref. 6 for RBaCo$_2$O$_{5+\delta}$. In case of Nd$_{1-x}$Ca$_x$BaCo$_2$O$_{5.5}$, the relation between α and σ is anomalous (α and σ decrease simultaneously), which precludes the use of the Jonker model. The grain boundary carrier scattering in our polycrystalline materials is likely the main mechanism that hinders the intrinsic relation between the Seebeck coefficient and the electrical resistivity.

IIIc. Magnetic properties

Temperature dependence of magnetization for Nd$_{1-x}$Ca$_x$BaCo$_2$O$_{5.5}$ that was measured on "field cooling" (FC) in a magnetic field of 1 kOe is presented in Fig. 7(a). A small anomaly in the paramagnetic susceptibility can be observed at T_{MI} (see: inset). This anomaly is associated with a spin state transition and will be discusses later. The characteristic temperatures determined from the $M(T)$ dependences are presented in Fig. 7(b).

For the undoped (x=0) material, the two transitions from paramagnetic (PM) to ferromagnetic (FM) and from FM to antiferromagnetic (AFM) state can be observed very close to each other, which manifests itself as the presence of a narrow cusp around T=250 K. Upon Ca doping, the PM/FM transition is increasing and approaches T_{MI}, which slightly decreases at the same time. The FM/AFM transition temperatures decrease in a more pronounced way and disappear for x≥0.1, above which all the compositions become

fully FM. A similar decrease of FM/AFM transition temperature has been observed for YBa$_{1-x}$Ca$_x$Co$_2$O$_{5.5}$ [16] at equivalent substitution levels x. Since the substitution of Ca for Ba is isovalent it should not change the oxidation state of Co indicating that the main mechanism for suppression of the FM/AFM transition in that case should be attributed to the local disorder on the Ba/Ca-site, which may also induce oxygen disorder. Charge doping by oxygen addition in GdBaCo$_2$O$_{5.5+\delta}$ leads also to suppression of the AFM phase, however, the FM/AFM transition temperature is suppressed only slightly before the oxygen defect induced disorder at $\delta \sim 0.05$ leads to compositional phase separation. It is possible that the similar disorder induced processes contribute to the suppression of the AFM state for our Nd$_{1-x}$Ca$_x$BaCo$_2$O$_{5.5}$ materials. However, this picture needs further clarification with respect to careful study of the samples total and local oxygen stoichiometry as well as presence of the anti-site defects on Ba- and Nd- sites for Ca substituted materials.

On the contrary to our samples, YBa$_{1-x}$Ca$_x$Co$_2$O$_{5.5}$ does not demonstrate an increase in T_C up to x=0.1. This is similar to oxygen addition in GdBaCo$_2$O$_{5.5+\delta}$ where despite the equivalent charge doping to our materials the local oxygen disorder causes decrease of T_C. The increase of T_C observed for our samples is therefore associated with the hole doping by Ca^{2+} for Nd^{3+} and creation of localized Co^{4+} ions. We argue that an alternative path to hole doping by oxygen defects introduces Co^{4+} ions, but also introduces disorder into the Co-O network by the formation of larger amount of CoO$_6$ octahedra at the expense of CoO$_5$ pyramids. This effect causes increasing delocalization of electrons across Co-O-Co bonds and lowering T_C.

The molar magnetic susceptibility, $\chi=M/H$, in the paramagnetic region, was used to determine the effective paramagnetic moment μ_{eff}, by fitting the Curie-Weiss formula $\chi = \chi_0 + (1/8) * \mu_{eff}^2 / (T - \Theta)$. In this formula χ_0 is a temperature-independent susceptibility, $\mu_{eff} = g\sqrt{S(S+1)}$ is the spin-only effective paramagnetic moment ($g = 2$ is the gyromagnetic factor and S is the effective spin) and Θ is the paramagnetic Curie-Weiss temperature. Before the analysis, the calculated paramagnetic contribution of Nd^{3+} ions was subtracted from the experimental data. We assume that Nd^{3+} ions in Nd$_{1-x}$Ca$_x$BaCo$_2$O$_{5.5}$ follow the Curie law $\chi_{Nd} = (1-x)*(1/8)*(\mu_{eff}^{Nd})^2/T$ with the value $\mu_{eff}^{Nd} = 3.5$.

The analysis of the Curie-Weiss behavior was performed separately for the two paramagnetic regions: below and above MIT. Different behavior of the parameters of the paramagnetic state below and above T_{MI}, commonly described as the change of slope of the inverse susceptibility at T_{MI}, is observed. The paramagnetic Curie-Weiss temperature Θ below T_{MI} is always positive and coincides with T_C with small deviations for larger x. This observation points to ferromagnetic interactions between $Co^{3+/4+}$ ions. For $T < T_{MI}$, χ_0 is negative (about -0.005 emu/mol), which is an indication of the presence of (diamagnetic) Co^{3+} ions that are in the LS state. For $T > T_{MI}$, the $M(T)$ dependences contain a significant paramagnetic temperature independent background χ_0, (1-4 10^{-3} emu/mol, presumably of the Pauli type for these conductive materials) associated with an unknown fraction of Co ions. The effective paramagnetic moments for the remaining fraction (following the Curie-Weiss law) of Co ions above T_{MI} are generally larger (5-7 μ_B), which is apparently associated with a transition of (some) Co^{3+} to higher spin states at T_{MI}. Θ is negative for most compounds with a tendency to change the sign to positive values for larger x. The scattering of the μ_{eff} values hinders the unambiguous determination of the Co spin state above T_{MI}.

The lines in Fig. 8(b) show the $\mu_{eff}(x)$ dependences calculated for different spin states of Co^{3+} and Co^{4+}, according to the formula $\mu_{eff}^2(x) = (2-x)\mu_{eff}^2(Co^{3+}) + x\mu_{eff}^2(Co^{4+})$. (Note that μ_{eff} is a paramagnetic moment for one formula unit, i.e., two cobalt ions.) Of all the simple models used, the best description of the observed $\mu_{eff}(x)$ dependence below T_{MI} is given by the model (Co3IS/LS+Co4LS), where Co^{3+} is in a combined spin state IS+LS in the 1:1 ratio (presumably one of the spin state for Co in the octahedra and one in the pyramids, but the magnetization measurements do not allow to differentiate between these two sites) and Co^{4+} is the LS spin state. A possible disproportionation of Co^{3+} ions into Co^{2+} and Co^{4+}, [7,28] does not change much the analysis since the paramagnetic moment of a Co^{2+}:HS and Co^{4+}:LS pair (4.24 μ_B) is only 6% higher than that of two Co^{3+}:IS ions.

Literature data for $RBaCo_2O_{5.5}$ support LS state for octahedral cobalt in the insulating phase (below T_{MI}) [3,6,31,32,33], however there are also present results suggesting IS state [34] or HS state. [35,36] For square pyramidal coordination either IS

state [3,6,31,32] or HS state [33,35,36] are proposed. The larger μ_{eff} above below T_{MI} suggests that that the fraction of Co^{3+} ions that are in the LS state below T_{MI} undergo a transition either to the IS or HS state.

Isothermal magnetization curves are presented in Fig. 9. In all the samples, below T_C, a clear hysteresis and no saturation up to 70 kOe can be observed. This is also true for the AFM region, although the shape of the magnetization curves is different. More complicated magnetization curves can also be observed (not shown), which indicate competing AFM and ferromagnetic interactions in these materials at low temperatures. For higher Ca concentrations, pronounced hysteresis can be observed at RT [Fig. 9(b)]. The parameters determined from $M(H)$ curves: M_{70} (high field magnetization in H=70 kOe) and M_{rem} (remanent magnetization in H=0) are presented in Fig. 9(c).

Magnetization values M_{70} and M_{rem} in Fig. 9(d) are lower than expected for full saturation of magnetic Co^{3+} and Co^{4+} ions. For example, if we analyze the model, which describes best the Co spin states in the paramagnetic state below MIT, i.e. Co^{3+} in the mixture of LS (S=0) + IS (S=1) states and Co^{4+} ions in the LS (S=1/2) state the expected saturation magnetization is M_s= 0(1-0.5x)+2(1-0.5x)+x=2μ_B. All compositions present low values of M_{rem}. A significant increase of the magnetization can be observed for x=0.08. This sample also demonstrates a large coercivity field $H_c\approx$13 kOe at 5 K, compared to other $Nd_{1-x}Ca_xBaCo_2O_{5.5}$ samples with H_c=2-5 kOe.

IV. Summary

In summary, we have synthesized and characterized a series of $Nd_{1-x}Ca_xBaCo_2O_{5.5}$ layered cobaltites with cation and vacancy ordering in the range of x=0-0.2. Hole doping by Ca substitution in this range preserves the metal insulator transition associated with an abrupt change of electrical and thermal transport properties and a Co^{3+} spin state transition. Our data indicate that a half of Co^{3+} ions undergoes a transition from the LS state to either IS or HS state on heating through T_{MI}. Upon Ca doping the carriers involved in the transport above T_{MI} change from electrons to holes, showing that a simple Coulomb blockade model is not in effect. The low temperature ferrimagnetic to

antiferromagnetic transition is completely suppressed above x=0.1. The ferrimagnetic transition temperature is increasing with Ca doping to values close T_{MI}, which slightly decreases. This is the largest enhancement of ferrimagnetic properties observed for these cobaltites. Since there are two alternative methods to effectively charge dope $RBaCo_2O_{5.5+\delta}$ layered cobaltites it may be interesting to study $Nd_{1-x}Ca_xBaCo_2O_{5.5+\delta}$ materials as a function of oxygen doping for a fixed amount of substitution x in order to clarify the effects of disorder and doping on magnetic and electronic properties.

References

[1] W. Zhou, Chem. Mater. **6**, 441 (1994).

[2] C. Martin, A. Maignan, D. Pelloquin, N. Nguyen, and B. Raveau, Appl. Phys. Lett. **71**, 1421 (1997).

[3] A. Maignan, C. Martin, D. Pelloquin, N. Nguyen, and B. Raveau, J. Solid State Chem. **142**, 247 (1999).

[4] D. Akahoshi and Y. Ueda, J. Solid State Chem. **156**, 355 (2001).

[5] E. Suard, F. Fauth, V. Caignaert, I. Mirebeau, and G. Baldinozzi, Phys. Rev. B **61**, R11871 (2000).

[6] A. A. Taskin, A. N. Lavrov, and Y. Ando, Phys. Rev. B **71**, 134414 (2005).

[7] A. Yu. Suntsov, I. A. Leonidov, M. V. Patrakeev,V. L. Kozhevnikov, J. Solid State Chem. **184**, 1951 (2011).

[8] F. Fauth, E. Suard, V. Caignaert, B. Domenges, I. Mirebeau, and L. Keller, Eur. Phys. J. B **21**, 163 (2001).

[9] T. Vogt, P. M. Woodward, P. Karen, B. A. Hunter, P. Henning, and A. R. Moodenbaugh, Phys. Rev. Lett. **84**, 2969 (2000).

[10] F. Fauth, E. Suard, V. Caignaert, and I. Mirebeau, Phys. Rev. B **66**, 184421 (2002).

[11] Yu. P. Chernenkov, V. P. Plakhty, V. I. Fedorov, S. N. Barilo, S. V. Shiryaev, and G. L. Bychkov, Phys. Rev. B **71**, 184105 (2005).

[12] V. P. Plakhty, Y. P. Chernenkov, S. N. Barilo, A. Podlesnyak, E. Pomjakushina, E. V. Moskvin, and S. V. Gavrilov, Phys. Rev. B **71**, 214407 (2005).

[13] Yu. P. Chernenkov, V. P. Plakhty, A. G. Gukasov, S. N. Barilo, S. V. Shiryaev, G. L. Bychkov, V. Hinkov, V. I. Fedorov, and V. A. Chekanov, Phys. Lett. A **365**, 166 (2007).

[14] D. D. Khalyavin, Phys. Rev. B **72**, 134408 (2005).

[15] D. D. Khalyavin, D. N. Argyriou, U. Amann, A. A. Yaremchenko, and V. V. Kharton, Phys. Rev. B **75**, 134407 (2007).

[16] G. Aurelio, J. Curiale, R. D. Sanchez, and G. J. Cuello, Phys. Rev. B **76,** 214417 (2007).

[17] A. Bharathi, P. Yasodha, N. Gayathri, A. T. Satya, R. Nagendran, N. Thirumurugan, C. S. Sundar, and Y. Hariharan, Phys. Rev. B **77**, 085113 (2008).

[18] Yan-kun Tang and C. C. Almasan, Phys. Rev. B **77**, 094403 (2008).

[19] Md. Motin Seikh, V. Caignaert, V. Pralong, and B. Raveau, Solid State Commun. **149**, 697 (2009).

[20] Md. Motin Seikh, V. Caignaert, V. Pralong, Ch Simon, and B. Raveau, J. Phys.: Condens. Matter **20**, 015212 (2008).

[21] Md. Motin Seikh, B. Raveau, V. Caignaert, and V. Pralong, J. Magn. Magn. Mater. **320**, 2676 (2008).

[22] A. Huq, J. P. Hodges, O. Gourdon, and L. Heroux, Zeitschrift für Kristallographie Proc., **1**, 127 (2011).

[23] A.C. Larson, R.B. Von Dreele, Los Alamos National Laboratory Report LAUR 86-748 (2004); B.H. Toby, J. Appl. Cryst. **34,** 210 (2001).

[24] D. Chernyshov, V. Dmitriev, E. Pomjakushina, K. Conder, M. Stingaciu, V. Pomjakushin, A. Podlesnyak, A. A. Taskin, and Y. Ando, Phys. Rev. B **78**, 024105 (2008).

[25] C. Frontera, J. L. García-Muñoz, O. Castaño, C. Ritter, and A. Caneiro, J. Phys.: Condens. Matter **20,** 104228 (2008).

[26] S. Streule, A. Podlesnyak, J. Mesot, M. Medarde, K. Conder, E. Pomjakushina, E. Mitberg, and V. Kozhevnikov, J. Phys.: Condens. Matter **17**, 3317 (2005).

[27] C. Frontera, J. L. García-Muñoz, and O. Castaño, J. Appl. Phys. **103**, 07F713 (2008).

[28] A. Maignan, V. Caignaert, B. Raveau, D. Khomskii, and G. Sawatzky, Phys. Rev. Lett. **93**, 026401 (2004).

[29] G. H. Jonker, Philips Res. Rep. **23**, 131 (1968); G. M. Choi, H. L. Tuller, and D. Goldschmidt, Phys. Rev. B **34**, 6972 (1986).

[30] S. R. Sehlin, H. U. Anderson, and D. M. Sparlin, Phys. Rev. B **52** 11681 (1995).

[31] M. Respaud, C. Frontera, J. L. García-Muñoz, M. A. G. Aranda, B. Raquet, J. M. Broto, H. Rakoto, M. Goiran, A. Llobet, and J. Rodriguez-Carvajal, Phys. Rev. B **64**, 214401 (2001).

[32] C. Frontera, J. L. García-Muñoz, A. Llobet, and M. A. G. Aranda, Phys. Rev. B **65**, 180405 (2002).

[33] J. F. Mitchell, J. Burley, and S. Short, J. Appl. Phys. **93**, 7364 (2003).

[34] Y. Moritomo, T. Akimoto, M. Takeo, A. Machida, E. Nishibori,M. Takata, M. Sakata, K. Ohoyama, and A. Nakamura, Phys. Rev. B **61**, R13325 (2000).

[35] Wu H. Wu, J. Phys.: Condens. Matter **15**, 503 (2003).

[36] W. R. Flavell, A. G. Thomas, D. Tsoutsou, A. K. Mallick, M. North, E. A. Seddon, C. Cacho, A. E. R. Malins, S. Patel, R. L. Stockbauer, R. L. Kurtz, and P. T. Sprunger, S. N. Barilo, S. V. Shiryaev, and G. L. Bychkov, Phys. Rev. B **70**, 224427 (2004).

Table I. Refined structural parameters for $Nd_{1-x}Ca_xBaCo_2O_{5.5}$, $0 \leq x \leq 0.06$ (RT). Space group *Pmmm*: Nd/Ca 2*p*; Ba 2*o*; Co1 (octahedral coordination) 2*r*; Co2 (square pyramidal coordination) 2*q*; O1 1*a*; O2 1*e*; O3 1*g*; O4 2*s*; O5 2*t*; O6 4*u*. Isotropic temperature factors, U_{iso}, are multiplied by 100.

Ca content (x)		0	0.02	0.04	0.06
a	(Å)	3.90123(2)	3.8985(5)	3.8989(4)	3.8984(2)
b	(Å)	7.8709(5)	7.8681(10)	7.8719(8)	7.8739(4)
c	(Å)	7.5928(5)	7.5895(10)	7.5911(8)	7.5925(4)
Unit cell volume	(Å³)	233.15(3)	232.80(5)	232.98(4)	233.05(2)
Nd/Ca	y	0.2721(2)	0.2724(4)	0.2725(3)	0.2715(2)
	U_{iso} (Å²)	0.36(3)	0.52(5)	0.33(4)	0.42(3)
Ba	y	0.2502(3)	0.2502(7)	0.2506(5)	0.2507(3)
	U_{iso} (Å²)	0.42(4)	0.73(9)	0.73(7)	0.40(4)
Co1 *oct*	y	0.5	0.5	0.5	0.5
	z	0.2476(6)	0.2462(12)	0.2460(9)	0.2479(6)
	U_{iso} (Å²)	0.38(6)	0.5(1)	0.5(1)	0.38(6)
Co2 *pyr*	y	0	0	0	0
	z	0.2534(6)	0.2517(11)	0.2553(9)	0.2531(5)
	U_{iso} (Å²)	0.34(6)	0.30(10)	0.36(9)	0.22(5)
O1	U_{iso} (Å²)	0.91(6)	1.3(1)	0.98(9)	0.98(6)
O2	U_{iso} (Å²)	0.53(6)	0.57(10)	0.66(9)	0.66(6)
O3	U_{iso} (Å²)	0.38(5)	0.44(10)	0.51(8)	0.43(5)
O4	z	0.3082(4)	0.3084(7)	0.3081(5)	0.3081(3)
	U_{iso} (Å²)	1.34(6)	1.55(11)	1.48(8)	1.34(5)
O5	z	0.2668(3)	0.2660(6)	0.2673(5)	0.2674(3)
	U_{iso} (Å²)	0.72(4)	0.92(8)	1.03(7)	0.78(4)
O6	y	0.2409(3)	0.2430(4)	0.2421(3)	0.2412(2)
	z	0.2880(2)	0.2876(4)	0.2878(3)	0.2878(2)
	U_{iso} (Å²)	0.90(3)	0.93(6)	0.93(5)	0.88(3)
Co1 – O2	(Å)	1.880(5)	1.868(9)	1.867(7)	1.882(4)
Co1 – O3	(Å)	1.916(5)	1.926(9)	1.928(7)	1.914(4)
Co1 – O5 x 2	(Å)	1.9561(4)	1.9551(8)	1.9562(6)	1.9548(4)
Co1 – O6 x 2	(Å)	2.063(2)	2.047(4)	2.055(3)	2.060(2)
Co2 – O1	(Å)	1.924(5)	1.91(1)	1.938(7)	1.922(4)
Co2 – O4 x 2	(Å)	1.995(1)	1.996(2)	1.990(2)	1.993(1)
Co2 – O6 x 2	(Å)	1.914(2)	1.931(4)	1.921(3)	1.918(2)
O2 – Co1 – O3	(deg)0	180	180	180	180
O5 – Co1 – Co5	(deg)	171.5(3)	171.2(6)	170.5(4)	171.3(3)
O6 – Co1 – Co6	(deg)	162.9(3)	162.3(5)	162.2(4)	163.1(3)
O4 – Co2 – O4	(deg)	155.9(3)	155.1(6)	156.8(5)	155.8(3)
O6 – Co2 – O6	(deg)	164.2(3)	163.8(5)	165.3(4)	164.2(3)
R_{wp} (%)		2.86	2.35	2.17	2.17
R_p (%)		3.93	5.31	3.35	3.74
χ^2		1.929	1.864	2.01	2.426

Table II. Refined structural parameters for $Nd_{1-x}Ca_xBaCo_2O_{5.5}$, $0.08 \le x \le 0.18$ (RT). Space group *Pmaa*: Nd/Ca 4*h*; Ba 4*g*; Co1 (octahedral coordination) 2*f*; Co2 (square pyramidal coordination) 2*e*; O1 2*e*; O2/O3 2*f*; O4 4*i*; O5 4*j*; O6/O7 4*k*. Isotropic temperature factors, U_{iso}, are multiplied by 100.

| Ca content		0.08	0.1	0.12	0.14	0.16	0.18
a	(Å)	7.79520(7)	7.79505(10)	7.79508(12)	7.7924(7)	7.79444(8)	7.80110(9)
b	(Å)	7.87538(8)	7.87608(11)	7.87672(13)	7.8745(7)	7.87535(9)	7.87333(9)
c	(Å)	7.59485(8)	7.59645(11)	7.59857(13)	7.5965(7)	7.59667(9)	7.60288(8)
Unit cell volume	(Å³)	466.249(8)	466.380(11)	466.550(13)	466.13(7)	466.314(9)	466.974(9)
Nd/Ca	*y*	0.2709(2)	0.2701(2)	0.2691(2)	0.2671(3)	0.2676(2)	0.2653(5)
	U_{iso} (Å²)	0.50(1)	0.48(2)	0.44(2)	0.52(4)	0.45(1)	0.43(5)
Ba	*y*	0.2511(3)	0.2505(4)	0.2498(3)	0.2512(5)	0.2502(4)	0.2484(7)
	U_{iso} (Å²)	0.61(2)	0.57(4)	0.55(4)	0.67(6)	0.67(3)	0.68(7)
Co1 *oct*	*y*	0.492(1)	0.492(1)	0.492(1)	0.506(2)	0.499(2)	0.496(1)
	z	0.2485(6)	0.2495(7)	0.2482(6)	0.2495(8)	0.2475(6)	0.2492(6)
	U_{iso} (Å²)	0.41(5)	0.33(7)	0.30(7)	0.33(11)	0.49(6)	-0.5(2)
	M_x (μ_B)	0.67(2)	1.01(2)	1.30(2)	1.44(2)	1.54(2)	1.64(2)
Co2 *pyr*	*y*	0.002(2)	0.006(1)	0.003(2)	0.005(2)	0.003(1)	0.002(1)
	z	0.2527(5)	0.2541(6)	0.2536(6)	0.2550(8)	0.2539(6)	0.2536(6)
	U_{iso} (Å²)	0.24(4)	0.20(6)	0.29(6)	0.23(10)	0.07(4)	-0.7(2)
	M_x (μ_B)	0.37(2)	0.71(2)	1.00(2)	1.24(2)	1.25(2)	1.51(2)
O1	U_{iso} (Å²)	0.95(4)	0.94(6)	0.87(5)	0.78(8)	0.74(4)	1.0(1)
O2	U_{iso} (Å²)	0.86(4)	0.72(5)	0.67(5)	0.75(8)	0.62(3)	0.1(1)
O3	U_{iso} (Å²)	0.54(4)	0.80(5)	1.12(6)	1.35(10)	1.23(5)	4.6(2)
O4	*z*	0.3074(3)	0.3080(4)	0.3070(3)	0.3054(5)	0.3054(3)	0.3031(4)
	U_{iso} (Å²)	1.39(3)	1.40(5)	1.30(5)	1.26(7)	1.26(4)	1.59(9)
O5	*z*	0.2671(3)	0.2678(3)	0.2691(3)	0.2693(5)	0.2710(3)	0.2730(4)
	U_{iso} (Å²)	1.03(3)	1.03(4)	0.99(4)	1.05(6)	1.14(3)	2.9(1)
O6	*y*	0.2482(4)	0.2482(5)	0.2460(6)	0.2465(9)	0.2481(5)	0.2454(8)
	z	0.2860(3)	0.2862(4)	0.2861(5)	0.286(1)	0.2862(3)	0.2884(4)
	U_{iso} (Å²)	0.49(2)	0.53(4)	0.47(4)	0.7(1)	0.50(2)	0.63(9)
O7	*y*	0.2330(4)	0.2329(6)	0.2355(7)	0.2357(11)	0.2349(5)	0.2403(9)
	z	0.2906(4)	0.2901(6)	0.2916(7)	0.2945(11)	0.2932(4)	0.2887(5)
	U_{iso} (Å²)	1.68(5)	1.45(7)	1.85(9)	1.6(2)	1.94(6)	3.6(1)
Co1-O2	(Å)	1.888(4)	1.896(5)	1.887(4)	1.896(6)	1.880(5)	1.895(5)
Co1-O3	(Å)	1.911(4)	1.904(5)	1.914(4)	1.904(6)	1.918(5)	1.908(5)
Co1-O5 x 2	(Å)	1.9550(4)	1.9549(5)	1.9563(5)	1.9545(7)	1.9567(5)	1.9589(5)
Co1-O6	(Å)	1.940(9)	1.94(1)	1.96(1)	2.06(2)	2.01(1)	1.997(12)
Co1-O7	(Å)	2.19(1)	2.19(1)	2.17(1)	2.07(2)	2.11(1)	2.10(1)
Co2-O1	(Å)	1.919(4)	1.930(5)	1.927(4)	1.938(6)	1.929(4)	1.929(5)
Co2-O4 x 2	(Å)	1.993(1)	1.992(1)	1.991(1)	1.986(2)	1.988(1)	1.986(1)
Co2-O6	(Å)	1.95(1)	1.93(1)	1.93(1)	1.91(2)	1.95(1)	1.94(1)
Co2-O7	(Å)	1.88(1)	1.90(1)	1.90(2)	1.92(2)	1.90(1)	1.93(1)
O2-Co1-O3	(deg)	176.1(5)	176(6)	176.1(6)	177.0(10)	177.4(6)	178.2(6)
O5-Co1-Co5	(deg)	170.9(3)	170.9(4)	170.0(3)	170.7(5)	169.6(3)	169.3(4)
O6-Co1-Co7	(deg)	163.1(3)	163.6(3)	162.8(3)	162.7(4)	162.1(3)	163.2(3)
O4-Co2-O4	(deg)	155.9(3)	156.1(3)	156.4(3)	157.6(4)	157.1(3)	158.2(3)
O6-Co2-O7	(deg)	163.7(3)	164.4(3)	163.9(3)	163.9(4)	163.6(3)	164.2(3)
R_{wp} (%)		2.57	2.75	3.38	3.08	3.48	4.71
R_p (%)		3.58	3.88	4.19	4.46	4.92	3.69
χ^2		2.034	1.983	2.323	2.394	2.838	1.634
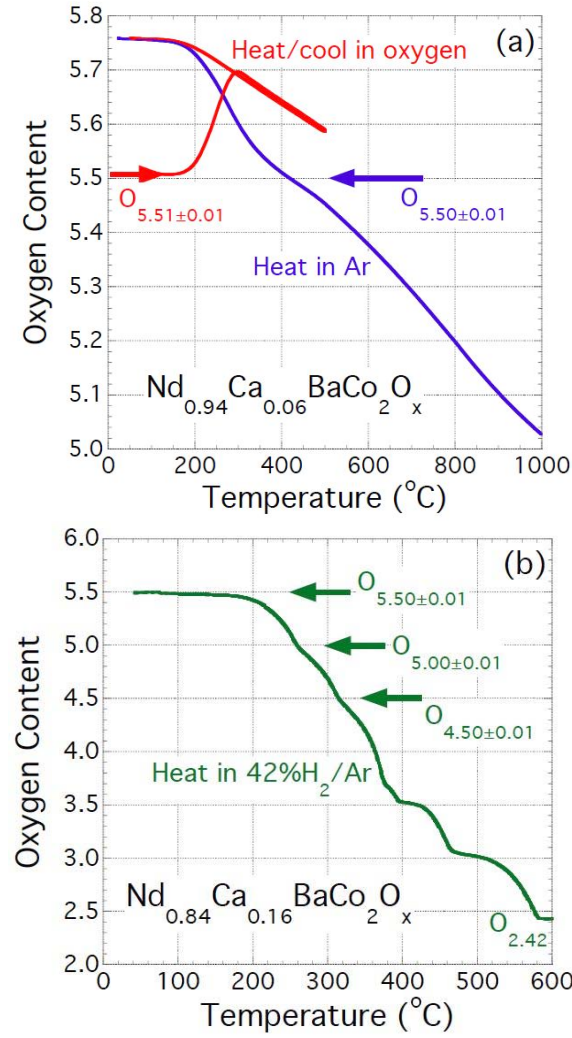
Fig. 1. (Color online) Oxygen content as a function of temperature for (a) $Nd_{0.94}Ca_{0.06}BaCo_2O_{5.51\pm0.01}$ during heating/cooling in oxygen and heating in Ar and (b) stoichiometric $Nd_{0.84}Ca_{0.16}BaCo_2O_{5.50\pm0.01}$ during heating in 42% H_2/Ar (note enhanced stability of oxygen composition at 5.00 and 4.50).
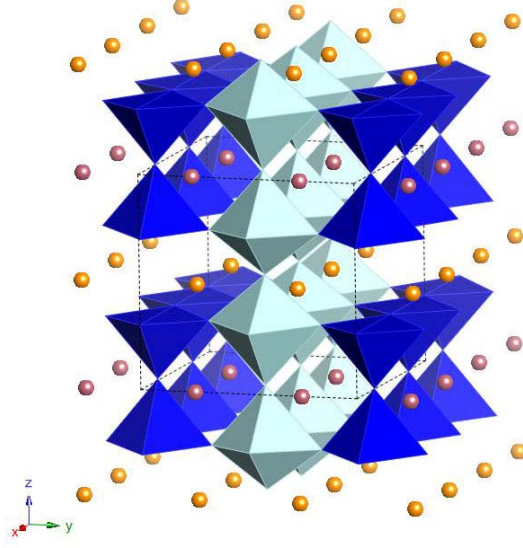
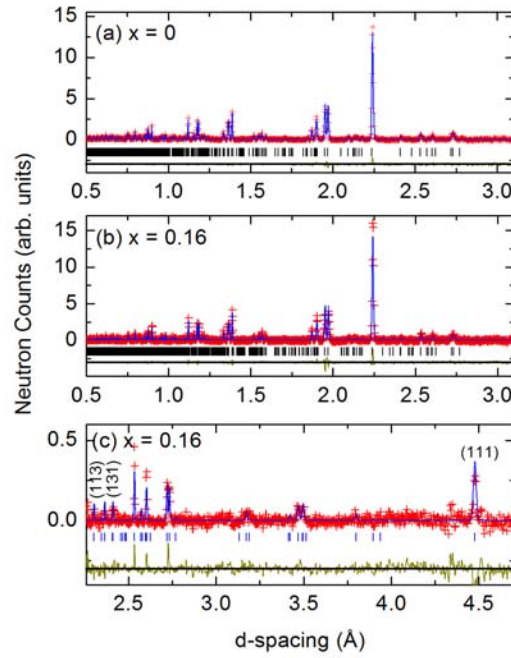Fig. 2. (Color online) Crystal structure of $Nd_{1-x}Ca_xBaCo_2O_{5.5}$.

Fig. 3. (Color online) Results of Rietveld analysis of neutron time of flight data for $NdBaCo_2O_{5.5}$ (a) and $Nd_{0.84}Ca_{0.16}BaCo_2O_{5.5}$ (b, c) at room temperature.
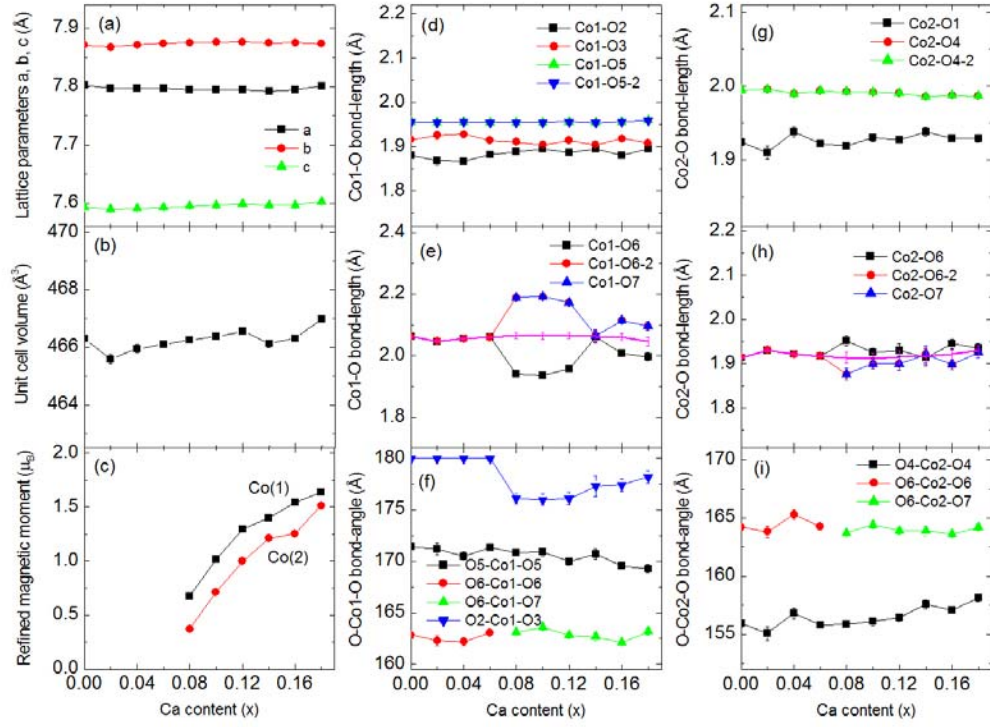
Fig. 4. (Color online) Refined structural parameters for $Nd_{1-x}Ca_xBaCo_2O_{5.5}$ as a function of Ca content.
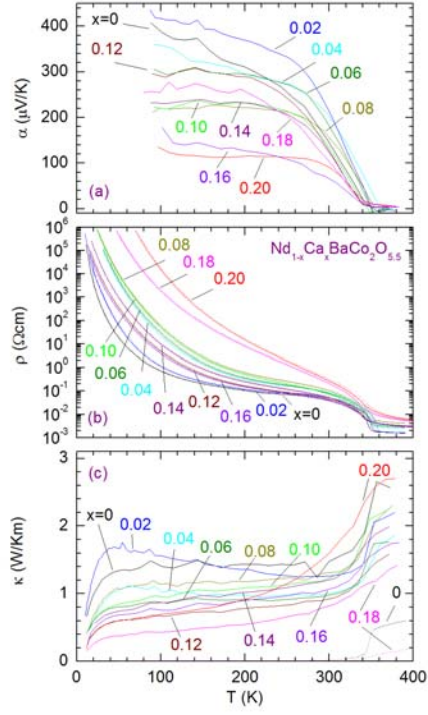
Fig. 5. (Color online) Temperature dependence of (a) the Seebeck coefficient , (b) electrical resistivity, and (c) thermal conductivity for $Nd_{1-x}Ca_xBaCo_2O_{5.5}$. Dashed lines in (c) represent the electronic contribution to thermal conductivity.
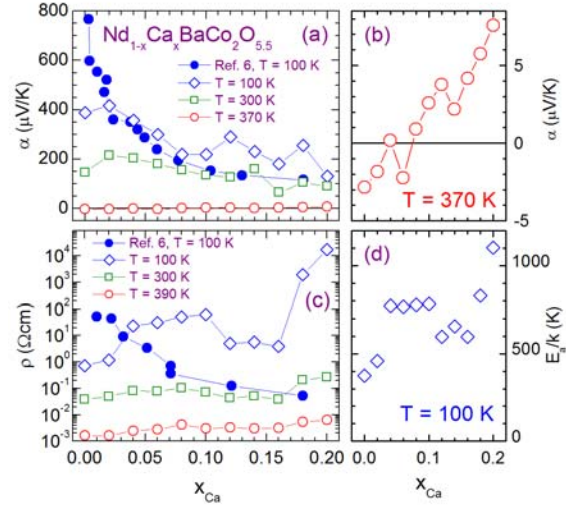
Fig. 6. (Color online) (a) The Seebeck coefficient below and above T_{MI} as a function of doping level (Ca concentration) in $Nd_{1-x}Ca_xBaCo_2O_{5.5}$; (b) The Seebeck coefficient at T=370 K; (c) The electrical resistivity below and above T_{MI}; (d) Activation energy as a function of Ca concentration. Full circles in (a,c) are plotted after Ref. 6 (see: text).
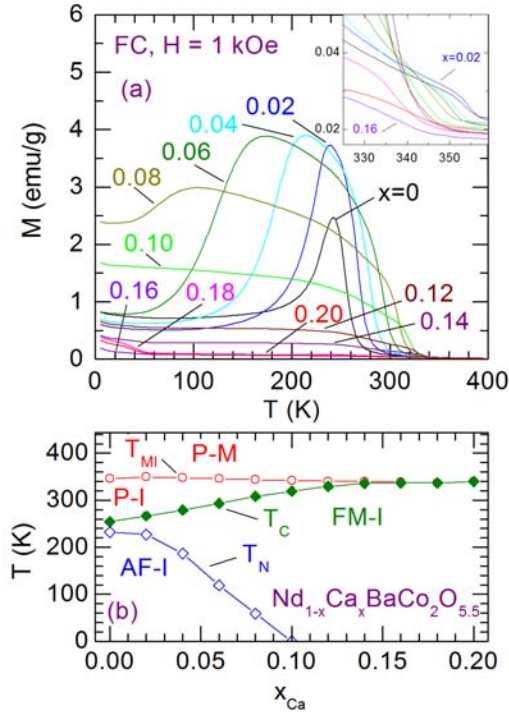
Fig. 7. (Color online) (a): Temperature dependence of magnetization for $Nd_{1-x}Ca_xBaCo_2O_{5.5}$ measured on "field cooling" (FC) in a magnetic field of 1 kOe. Inset: same data in the vicinity of T_{MI}. (b): The phase diagram: P-M is the paramagnetic metallic phase, P-I is the paramagnetic insulating phase, FM-I is the ferrimagnetic insulating phase, and AF-I is the antiferromagnetic insulating phase. The main transition temperatures T_{MI}, T_C, and T_N are plotted.
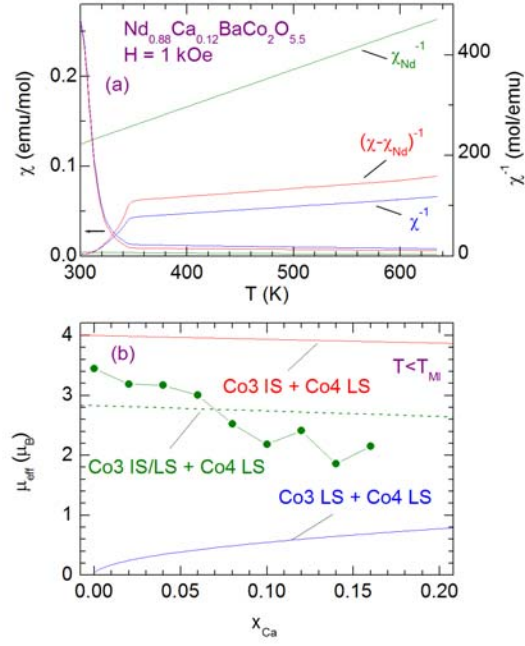
Fig. 8. (Color online) (a) The magnetic susceptibility of $Nd_{1-x}Ca_xBaCo_2O_{5.5}$ for x=0.12, (b) the effective paramagnetic moments μ_{eff} below T_{MI} as a function of the Ca content (see: text) The lines denote several models for $\mu_{eff}(x)$ with different spin states for $Co^{4+/3+}$: high spin HS, intermediate spin IS, and low spin LS.
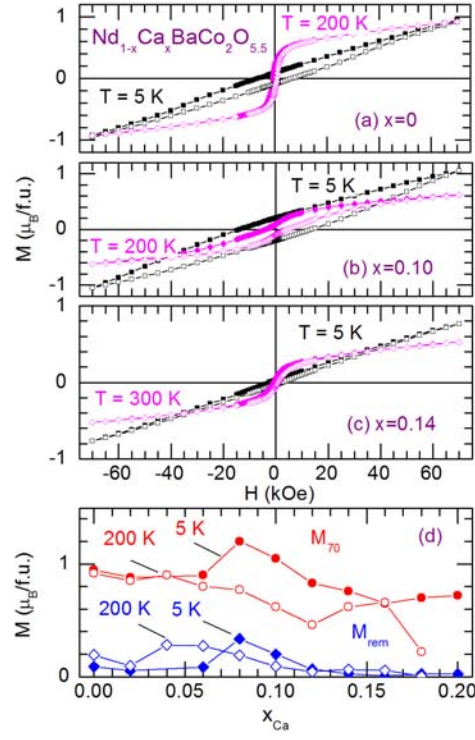
Fig. 9. (Color online) Magnetic hysteresis curves for x=0 (a), x=0.10 (b), and x=0.14 (c) samples.